Chin. J. Astron. Astrophys. Vol. 7 (2007), No. 3, 335–344
(*http://www.chjaa.org*)

Chinese Journal of
Astronomy and
Astrophysics

X-Ray Properties of the Point Source Population in the Spiral Galaxy NGC 5055 (M63) with *Chandra* *

Bing Luo[1], Ji-Yao Chen[1], Zhong-Li Zhang[2], Yu Wang[2], Jing-Ying Wang[2] and Hai-Guang Xu[2]

[1] Department of Physics, Fudan University, Shanghai 200433; *wenyu_wang@sjtu.edu.cn*
[2] Department of Physics, Shanghai Jiao Tong University, Shanghai 200240

Received 2006 September 11; accepted 2006 October 16

Abstract Using *Chandra* ACIS S3 data we studied the X-ray properties of low-and high-mass X-ray binary populations in the nearby spiral galaxy NGC 5055. A total of 43 X-ray point sources were detected within two effective radii, with 31 sources located on the disk and the rest 12 sources in the bulge. The resolved point sources dominate the X-ray emission of the galaxy, accounting for about 80% of the total counts in 0.3–10 keV. From spectral fittings we calculated the 0.3–10.0 keV luminosities of all the detected X-ray point sources and found that they span a wide range from a few times 10^{37} erg s^{-1} to over 10^{39} erg s^{-1}. After compensating for incompleteness at the low luminosity end, we found that the corrected XLF of the bulge population is well fitted with a broken power-law with a break at $1.57^{+0.21}_{-0.20}\times 10^{38}$ erg s^{-1}, while the profile of the disk population's XLF agrees with a single power-law distribution of slope $0.93^{+0.07}_{-0.06}$. The disk population is significantly richer at $\gtrsim 2\times 10^{38}$ erg s^{-1} than the bulge population, indicating that the disk may have undergone relatively recent, strong starbursts that significantly increased the HMXB population, although ongoing starbursts are also observed in the nuclear region. Similar XLF profiles of the bulge and disk populations were found in M81. However, in most other spiral galaxies different patterns of spatial variation of the XLF profiles from the bulge to the disk have been observed, indicating that the star formation and evolution history may be more complex than we have expected.

Key words: galaxies: individual (NGC 5055)—X-ray:binaries—stars: luminosity function—stars: formation

1 INTRODUCTION

The study of X-ray properties of bright point sources in spiral galaxies, most of which are low-mass X-ray binaries (LMXBs) or high-mass X-ray binaries (HMXBs), may provide us with valuable observational constraints on the star formation and evolution history in the disk and bulge of the host galaxy. With the superb high spatial resolution of the *Chandra* X-ray Observatory, a large population of X-ray point sources has been resolved for the first time in some nearby spiral galaxies. In a few specific cases, distinct X-ray characteristics have been revealed for sources located in the bulge and in the disk, which can be interpreted as evidence for spatial variation of stellar population composition resulting from differences in the star formation history (e.g., Tennant et al. 2001; Kong et al. 2002; Soria & Kong 2002). In this paper we present a study of the *Chandra* point sources in the nearby starburst galaxy NGC 5055 (M63; SA(rs)bc). The galaxy is one of the prototype Arm Class 3 flocculent galaxies (Elmegreen & Elmegreen 1987), and it shows a regular, two-arm spiral structure to a radius of 4.0 kpc in the near-infrared band. The optical center of the galaxy is identified to be at RA=$13^{\rm h}15^{\rm m}49.25^{\rm s}$, Dec=+$42^{\rm d}01^{\rm m}49.3^{\rm s}$ (J2000, Maoz et al. 1996). The LINER nucleus

* Supported by the National Natural Science Foundation of China.

is UV bright and is surrounded by luminous young star clusters, showing clear stellar absorption signatures (Maoz et al. 1998; Leitherer et al. 2002). The inclination and position angles of the galaxy are deduced to be 58° and 103°, respectively (Garcia-Gomez & Athanassoula 1991). We organize this paper as follows. In Section 2, we describe the observation and data reduction. In Section 3 we present our imaging analysis. In Section 4, we investigate the X-ray properties of the detected point sources, including both temporal and spectral analyses and we calculate the hardness ratios and X-ray luminosity functions (XLFs). Finally, we discuss and summarize the results in Sections 5 and 6, respectively. Throughout the paper, we quote errors at the 90% confidence level unless mentioned otherwise. We adopt a distance of 7.2 Mpc to NGC 5055 (Michele & Serra 1997), calculated from its redshift ($z = 0.001681$) for cosmological parameters $H_0 = 70\,\mathrm{km\ s^{-1}\,Mpc^{-1}}$, $\Omega_m = 0.3$ and $\Omega_\Lambda = 0.7$. At this distance $1'$ corresponds to about 2.1 kpc.

2 OBSERVATION AND DATA REDUCTION

NGC 5055 was observed by *Chandra* with the CCD 0, 1, 2, 3, 6 and 7 of the *Chandra* Advanced CCD Imaging Spectrometer (ACIS) on two separate occasions, one on 2001 August 27, for a total exposure of 28.4 ks, one on 2001 April 15, for a shorter duration of 2.4 ks. The events were telemetered in faint mode and the data were collected with a frame time of 3.2 s. The CCD temperature was set at -120 °C. In the August 27 observation from which the data of this work were drawn, the center of galaxy was positioned on the ACIS S3 chip (CCD 7) with an offset of $31''$ from the nominal pointing for the S3 chip, so nearly all the emission of the galaxy was covered by the S3 chip. In the analysis that follows, we used the CIAO software version 2.3 to process the data extracted from the S3 chip only. In order to apply the latest calibration (CALDB version 3.0), we started with the Level-1 data. We kept events with ASCA grades 0, 2, 3, 4 and 6, and excluded bad pixels, bad columns, and columns adjacent to bad columns and node boundaries. In order to identify occasional periods of high background, we extracted the lightcurve of the source-free regions on the S3 chip in 2.5–7.0 keV where the background flares are expected to be most visible. We found that up to about 5% of the total exposure time was affected by high background flares. After excluding the contaminated intervals we obtained a clean exposure of 27.0 ks for the analysis.

3 X-RAY IMAGE

In Figure 1a we contour the *Chandra* S3 image of NGC 5055 in 0.3–10.0 keV on a logarithmic scale. The image has been corrected for both exposure and background, and has been smoothed by using a minimum signal-to-noise ratio of 3 and a maximum signal-to-noise ratio of 5 per beam. We find that the X-ray emission from the galaxy is dominated by a large population of X-ray point sources, which contributes about 80% of the total counts of the galaxy in 0.3–10.0 keV. The diffuse X-ray emission is nearly symmetric within about $20''$, and is slightly elongated in east-west direction in outer regions. No diffuse X-ray is significantly detected beyond $\simeq 33''$, which is approximate the size of the bulge ($\simeq 35''$, Baggett et al. 1998). We find that the diffuse X-ray emission is peaked at RA=$13^{\rm h}15^{\rm m}49.3^{\rm s}$, DEC=+$42^{\rm d}01^{\rm m}45.5^{\rm s}$ (J2000) where a bright nuclear X-ray point source is detected. The position of the X-ray peak also coincides with the optical and infrared centers of the galaxy to within $0.5''$. In Figure 1b we show the optical image drawn from the Digital Sky Survey (DSS) on a linear scale, on which the locations of the 43 detected X-ray sources are marked with circles for comparison (Sect. 4.1).

4 X-RAY POINT SOURCES

4.1 Detections

We detected X-ray point sources on the ACIS S3 image using the CIAO tool celldetect with a signal-to-noise threshold of 3. We first restricted the detections in 0.3–10.0 keV, and then crosschecked the results in 0.5–7.0 keV. We also have crosschecked the results by using the wavelet-based CIAO tool wavedetect, and by visual examination. On the whole S3 CCD, 46 sources are detected, of which 43 sources are located within the two effective radii (one effective radius = $1R_{\rm e}$ = $1.6'$, Thornley 1996). In this work we focus our study on these 43 sources only. The spatial distribution of the 43 sources shows a clear concentration towards the galaxy center, indicating that most of them are physically associated with the galaxy. Based on the results of the deep *Chandra* observations of the blank fields (Mushotzky et al. 2000), we performed Monte-Carlo simulations and found that only few ($\lesssim 5$) of the 43 point sources may be unrelated background sources. By overlaying the positions of these sources on the DSS image (Fig. 1b), we find that 31 of the 43 sources

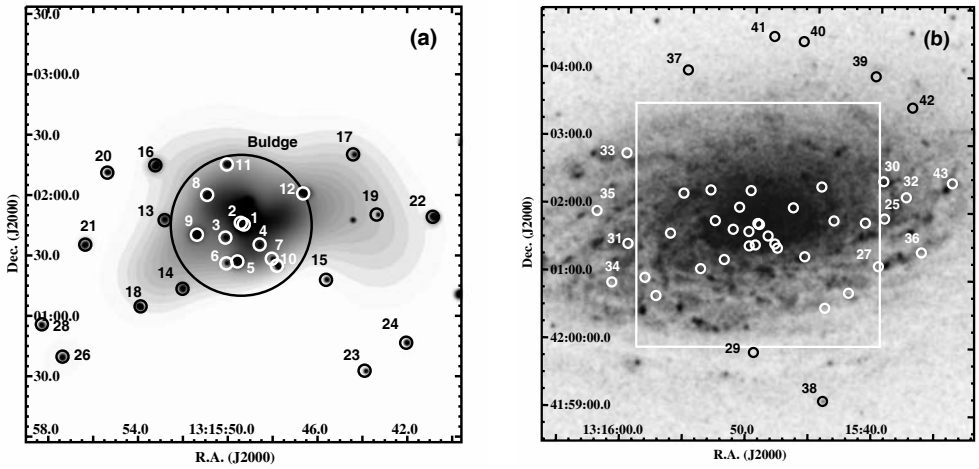

Fig. 1 (a): X-ray image of the central $3.6' \times 3.6'$ region of NGC 5055 in 0.3–10 keV in logarithmic scale, which has been smoothed with a minimum significance of 3 and a maximum significance of 5, and has been corrected for both exposure and background. We show the bulge region with a circle. (b): DSS blue image with the field of view of (a) marked with a box. On both images the detected X-ray point sources are marked with small circles.

are detected on the disk with a tendency to reside on the spiral arms. The rest 12 sources are detected in the bulge, of which up to about 1 source may be a disk population source that is misclassified into the bulge population due to projection effect. At the X-ray peak a nuclear source is detected which, however, does not have the highest count rate among the detected sources. We list the properties of the 43 sources in Table 1, ordered in increasing projected distance from the center of the galaxy.

4.2 Temporal Variabilities

After removing the intervals of strong background flares, we extracted the 0.3–10.0 keV lightcurves of the detected sources that each have more than 60 counts (Fig. 2). We calculated the Kolmogoroff-Smirov (K-S) statistic for each of the lightcurves against the null hypothesis that the count rate of the source is temporally invariant over the effective exposure time. If the source is temporally invariant, the cumulative fraction of the count is a diagonal from 0 to 1. Evidence for significant temporal variations on the 90% confidence level was found in Src 22 (243 counts), Src 35 (600 counts) and Src 38 (102 counts, see Fig. 3). This is not likely to be caused by variations in the local background, since the K-S test gives negative results in the background variability. For the central source (Src 1), the temporal variability is less significant in the K-S test, possibly because the K-S test is most sensitive around the median value of the independent variable. However, by calculating the variability parameter $S = (f_{\max} - f_{\min})/\sqrt{\sigma^2_{f_{\max}} + \sigma^2_{f_{\min}}} = 1.1$, where $f_{\max}$ and $f_{\min}$ are the maximum and minimum count rates, respectively, and $\sigma_{f_{\max}}$ and $\sigma_{f_{\min}}$ are the corresponding errors, we find that Src 1 is marginally variable on timescales of $1 \sim 5$ hr during which its count rate changed by about 50%.

4.3 Hardness Ratios

Since the background-corrected count rates of most of the resolved X-ray point sources are low, which make it impossible to carry out spectral analysis for each source, we turned to a study of the hardness ratios of all the sources. Two hardness ratios are defined: $H_{21} = (M - S)/(M + S)$ and $H_{31} = (H - S)/(H + S)$, where S, M and H are the background-corrected counts extracted in 0.3–1.0 keV (S), 1.0–2.0 keV (M) and 2.0–10.0 keV (H), respectively. The same approach has been adopted in earlier works (e.g., Sarazin et al. 2000). We list the calculated hardness ratios and the 1σ errors in Columns 7 and 8 of Table 1, and plot H_{31} against H_{21} in Figure 4. In the figure we show the predicted hardness ratio distributions for two

Table 1 X-ray Properties of the Detected Sources[a]

Src. No.	R.A.(J2000) (h:m:s)	Dec.(2000) (d:m:s)	count rate (10^{-3} cnt s^{-1})	d (arcsec)	$L_{\rm X}$ (0.3–10.0 keV) (10^{38} erg s^{-1})	$H_{21}^{\rm b}$	$H_{31}^{\rm c}$	notes[d]
1	13:15:49.287	+42:01:45.41	6.70±0.51	0	3.83	0.17 ± 0.04	-0.14 ± 0.04	b, c, v
2	13:15:49.423	+42:01:46.23	2.88±0.34	1.727	1.44	0.51 ± 0.11	0.87 ± 0.03	b,
3	13:15:50.109	+42:01:38.90	0.53±0.14	11.23	0.30	0.45 ± 0.17	0.65 ± 0.11	b,
4	13:15:48.581	+42:01:35.48	0.46±0.13	12.66	0.24	0.66 ± 0.16	0.74 ± 0.12	b
5	13:15:49.570	+42:01:27.06	4.51±0.40	18.61	2.56	0.76 ± 0.05	0.86 ± 0.03	b
6	13:15:50.061	+42:01:26.12	0.99±0.19	21.12	0.58	-0.56 ± 0.08	-1 ± 0.01	b, s
7	13:15:48.033	+42:01:28.42	0.56±0.15	21.99	0.32	-0.77 ± 0.08	-1 ± 0.01	b, s
8	13:15:50.923	+42:02:00.13	3.76±0.37	23.42	2.16	0.25 ± 0.06	0.06 ± 0.06	b
9	13:15:51.380	+42:01:40.38	7.51±0.52	23.86	4.16	-0.89 ± 0.02	-1 ± 0.01	b, s, v
10	13:15:47.807	+42:01:24.85	3.19±0.34	26.35	1.79	0.30 ± 0.07	0.51 ± 0.05	b
11	13:15:50.042	+42:02:15.21	2.80±0.32	30.96	1.60	0.28 ± 0.06	-0.02 ± 0.07	b
12	13:15:46.642	+42:02:00.89	3.37±0.36	33.28	1.92	-0.63 ± 0.04	-0.98 ± 0.01	b, s, v
13	13:15:52.813	+42:01:47.54	0.67±0.15	39.35	0.37	-0.27 ± 0.11	-1 ± 0.01	s
14	13:15:52.013	+42:01:13.47	1.05±0.20	44.07	0.61	-0.55 ± 0.08	-1 ± 0.01	s
15	13:15:45.619	+42:01:17.90	0.39±0.12	49.26	0.21	-0.59 ± 0.13	-0.77 ± 0.09	s
16	13:15:53.232	+42:02:14.79	8.87±0.57	52.87	5.10	0.10 ± 0.03	-0.31 ± 0.03	
17	13:15:44.417	+42:02:20.17	0.58±0.15	64.43	0.34	-0.17 ± 0.13	-0.47 ± 0.11	
18	13:15:53.889	+42:01:04.68	4.83±0.42	65.49	2.80	0.62 ± 0.04	0.58 ± 0.05	
19	13:15:43.364	+42:01:50.30	0.73±0.16	66.17	0.42	-1 ± 0.01	-1 ± 0.01	s
20	13:15:55.369	+42:02:11.11	0.84±0.17	72.47	0.46	0.66 ± 0.11	0.70 ± 0.09	
21	13:15:56.358	+42:01:35.35	1.42±0.23	79.43	0.83	0.33 ± 0.09	0.33 ± 0.09	
22	13:15:40.858	+42:01:49.16	8.71±0.56	93.98	5.02	0.16 ± 0.03	-0.22 ± 0.04	v
23	13:15:43.900	+42:00:32.75	0.55±0.14	94.25	0.31	0.86 ± 0.08	0.73 ± 0.14	
24	13:15:42.048	+42:00:46.67	0.68±0.15	99.78	0.37	0.05 ± 0.12	-0.62 ± 0.10	
25	13:15:39.338	+42:01:53.27	5.89±0.46	111.1	3.42	0.66 ± 0.03	0.43 ± 0.05	
26	13:15:57.370	+42:00:39.78	1.02±0.21	111.4	0.65	-0.14 ± 0.10	-0.19 ± 0.09	
27	13:15:39.739	+42:01:11.00	5.79±0.46	111.8	3.36	0.24 ± 0.04	-0.33 ± 0.04	
28	13:15:58.286	+42:00:55.74	0.87±0.18	111.9	0.50	0.49 ± 0.11	0.46 ± 0.11	
29	13:15:49.488	+41:59:51.84	2.16±0.18	113.5	1.25	0.36 ± 0.07	0.05 ± 0.08	
30	13:15:39.496	+42:02:26.35	2.43±0.30	116.5	1.41	0.75 ± 0.05	0.74 ± 0.05	
31	13:15:59.716	+42:01:25.17	0.45±0.13	117.9	0.26	1 ± 0.01	1 ± 0.01	
32	13:15:37.668	+42:02:12.76	1.46±0.23	132.3	0.84	0.24 ± 0.09	0.02 ± 0.09	
33	13:16:00.013	+42:02:45.36	0.82±0.17	133.6	0.45	0.05 ± 0.11	-0.68 ± 0.09	
34	13:16:00.916	+42:00:50.72	0.46±0.13	140.6	0.26	0.80 ± 0.10	0.63 ± 0.17	
35	13:16:02.251	+42:01:53.63	21.4±0.88	144.6	12.49	0.48 ± 0.02	-0.19 ± 0.03	v
36	13:15:36.348	+42:01:24.17	1.32±0.22	145.7	0.75	0.53 ± 0.10	0.66 ± 0.07	
37	13:15:55.308	+42:04:00.39	1.29±0.22	150.7	0.74	0.22 ± 0.09	-0.15 ± 0.10	
38	13:15:43.878	+41:59:10.46	3.50±0.35	166.2	2.02	0.01 ± 0.05	-0.43 ± 0.05	v, u
39	13:15:40.339	+42:03:59.03	0.74±0.16	166.6	0.44	0.59 ± 0.10	0.39 ± 0.13	
40	13:15:46.141	+42:04:28.37	0.77±0.17	166.6	0.45	0.32 ± 0.11	-0.10 ± 0.13	
41	13:15:48.505	+42:04:32.15	1.01±0.19	166.9	0.59	0.34 ± 0.11	0.28 ± 0.11	
42	13:15:37.359	+42:03:32.19	1.21±0.21	170.4	0.71	0.54 ± 0.08	0 ± 0.12	
43	13:15:34.029	+42:02:26.31	0.61±0.15	174.8	0.29	0.48 ± 0.15	0.53 ± 0.14	

[a] The columns are : (1) source number; (2)–(3): right ascension and declination (J2000); (4) count rate and its error; (5) projected distance *d* to the center of the galaxy; (6) intrinsic X-ray luminosity L_X, assuming that the source is located at the distance of NGC 5055 and only subjected to the Galactic absorption (1.31×10^{20} cm^{-2}, Dickey & Lockman 1990); (7)–(8): hardness ratios and the 1σ errors (Sect.4.3); and (9) notes. [b, c] H_{21} = (M-S)/(M+S), H_{31} =(H-S)/(H+S) [d], abbreviations are b: source in bulge; c: central source; s: candidate of supersoft source; u: ultra luminous X-ray source; and v: source shows temporal variability.

absorbed power-law models with column densities of 1.31×10^{20} cm^{-2} (the Galactic value, Dickey & Lockman 1990) and 3.93×10^{20} cm^{-2}, for photon indices of $\Gamma = 0.0,\ 1.0,\ 2.0,\ 3.0$ and 4.0, as well as for an absorbed blackbody model with the Galactic absorption and for temperatures of $kT = 0.5,\ 0.4,\ 0.3,\ 0.2$ and 0.1 keV.

We find that the distribution of the colors is similar to that of M31 (Kong et al. 2002) and the nearly face-on, gas-rich spiral galaxy M83 (Soria & Wu 2003). Most of the sources lie in a broad diagonal band extending from $(H_{21}, H_{31}) = (-1, -1)$ to (1,1). One source (Src 19) located at a moderate distance ($1.1'$) to the galaxy center has hardness ratios of about $(-1, -1)$ and is thus identified as a supersoft source (SSS).

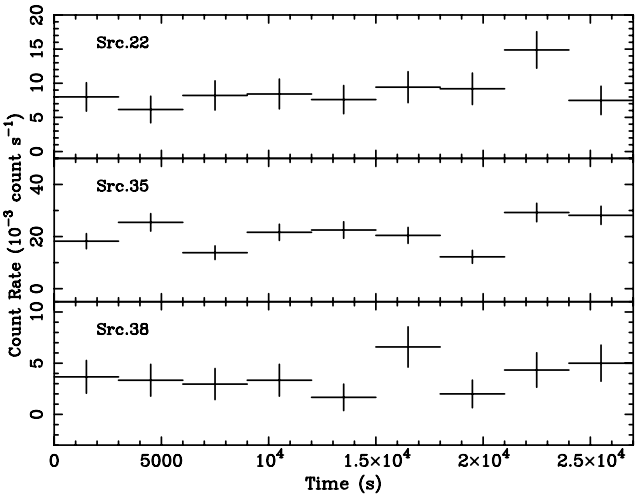

Fig. 2 Background-corrected lightcurves of Src 22, Src 35 and Src 38.

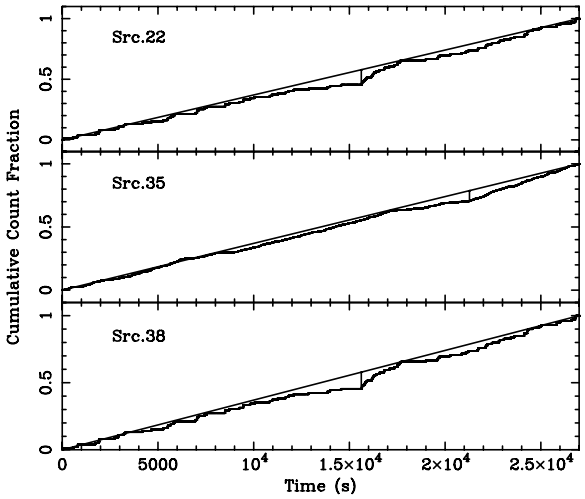

Fig. 3 Results of Kolmogoroff-Smirov test for the lightcurves of Src 22, Src 35 and Src 38.

If the selection criterions of Supper et al. (1997) and Kahabka (1999) are applied, five other sources (Src 6, 7, 9, 13 and 14) can be identified as SSS candidates since they satisfy $H_{31} + \sigma_{H_{31}} < -1$ and $H_{21} < 0$, or $H_{21} + \sigma_{H_{21}} < -0.8$. If we relax the selection limit to $H_{21} < 0.5$ and $H_{31} < 0.5$ (e.g. Swartz et al. 2002), then Src 12 and 15 can also be classified as SSS candidates. As is shown in Figure 4 the hardness ratios of these supersoft sources can approximately be described with an absorbed black-body model with temperatures ranging from about 0.2 to 0.3 keV. Src 31 has a hardness ratio of (1,1), which appears to have been heavily absorbed by a column density significantly larger than the Galactic value. Since Src 31 is located far away from the center of the galaxy ($d > 110''$) and its hardness ratios agree with those expected by an absorbed power-law model with an absorption of $\geq 0.4 \times 10^{22}$ cm^{-2} and a photon index of $\Gamma \sim 0$, it is probably an unrelated background AGN.

For comparison, within the $2R_{\rm e}$ region the measured mean hardness ratios for the total X-ray emission of the galaxy are $(H_{21}, H_{31}) = (-0.28, 0.18)$. For the same region, the mean hardness ratios are $(H_{21}, H_{31}) = (-0.14, 0.13)$ for all the resolved X-ray point sources and $(-0.46, 0.23)$ for the unresolved diffuse emission.

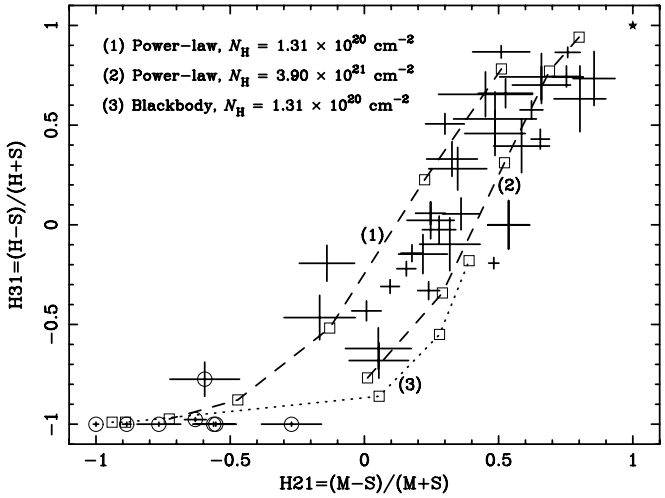

Fig. 4 Color-color diagram of the resolved point sources. Super soft sources (SSSs) are marked with open circles and the hardest source, an open star. Model predictions are shown with dashed and dotted lines. From top of the figure downwards, open rectangles on the lines indicate the values of photon indices of $\Gamma = 0.0,\ 1.0,\ 2.0,\ 3.0$ and 4.0 for two power-law models, and for temperatures of $kT = 0.5,\ 0.4,\ 0.3,\ 0.2, 0.1$ keV for the blackbody model.

4.4 Spectral Analysis

We first extracted and studied the cumulative spectrum of all the 42 off-center point sources resolved within $2R_{\rm e}$. The backgrounds were extracted from a carefully selected annulus around each source. By applying the latest CALDB we corrected for the charge transfer inefficiency (CTI) and the continuous degradation in the ACIS quantum efficiency, which is especially severe at lower energies. To avoid effects of calibration uncertainties at lower energies and instrumental background at higher energies we restricted the spectral analysis to the 0.7–7.0 keV energy band. We found that the cumulative spectrum cannot be fitted with a single absorbed power-law model, if the absorption is fixed at the Galactic value. When the absorption was allowed to vary, however, the absorbed power-law model can give an acceptable fit ($\chi^2/{\rm dof} = 152.7/116$). The resulting absorption is $(0.14 \pm 0.01) \times 10^{22}\,{\rm cm}^{-2}$ and the photon index is 2.05 ± 0.06. With these parameters the total flux of all the 42 off-center sources in 0.3–10.0 keV was calculated to be 7.79×10^{-13} erg s^{-1} cm^{-2}. We also divided the resolved off-center sources into a disk and a bulge population and studied their cumulative spectra in 0.7–7.0 keV. The cumulative spectrum of the disk population can be marginally fitted with an absorbed power-law model with an absorption of $(0.27 \pm 0.03) \times 10^{22}\,{\rm cm}^{-2}$ and a photon index of 2.45 ± 0.08 ($\chi^2/{\rm dof} = 138.9/112$). The spectrum of the bulge population, on the other hand, can be well fitted with a model that consists of a power-law component and a black body component, both subjected to a common absorption that is consistent with the Galactic value ($\chi^2/{\rm dof} = 60.1/55$). The obtained photon index and temperature are $\Gamma = 1.36 \pm 0.13$ and $kT = 0.12 \pm 0.01$ keV.

By excluding all the detected point sources we examined the spectrum of the diffuse emission in $< 2R_{\rm e}$ contributed by both the unresolved point sources and the inter-stellar medium (ISM). The background was extracted in a source-free boundary region on the S3 chip as far away as possible from the galaxy. We first attempted to fit the spectrum with an absorbed power-law or an absorbed MEKAL model, but neither of them gives an acceptable fit to the data, unless the absorption is allowed to increase to unreasonable, physically meaningless values. So we attempted to apply a model that consists of a MEKAL component to represent the emission of the hot ISM, and a power-law component to represent the contribution of X-ray binaries, with both components subjected to a common absorption. Since the abundance of the MEKAL component is poorly constrained, we tentatively fixed it at 0.1 $Z_{\odot}$, the value obtained by Tyler et al. (2004) for the central region of NGC 5055. We found that when the absorption is fixed at the Galactic value, the

Table 2 Spectral Fittings of the Brightest Sources [a]

	Power-law Model				DBB Model			
Src. No.	$N_{\rm H}$ (10^{22} cm^{-2})	α	χ^2/dof	$F_{\rm X}/10^{-14}$ (erg s^{-1} cm^{-2})	$N_{\rm H}$ (10^{22} cm^{-2})	$T_{\rm in}$ (keV)	χ^2/dof	$F_{\rm X}/10^{-14}$ (erg s^{-1} cm^{-2})
1	0.013 / fixed	1.61 ± 0.15	7.7/7	5.10	0.013 / fixed	0.94 ± 0.13	3.5/7	3.62
5	0.013 / fixed	0.23 ± 0.14	3.5/4	7.64	–	–	–	–
8	0.013 / fixed	1.41 ± 0.16	1.2/3	3.95	0.013 / fixed	1.23 ± 0.22	1.9/3	2.67
9	–	–	–	–	0.013 / fixed	0.15 ± 0.01	5.0/5	4.29
16	0.013 / fixed	1.67 ± 0.12	7.8/9	7.18	0.013 / fixed	0.96 ± 0.10	7.9/9	5.18
18	0.013 / fixed	0.15 ± 0.27	1.4/3	17.14	0.20 ± 0.15	3.02 ± 7.34	0.39/2	7.48
22	0.013 / fixed	1.46 ± 0.13	10.6/9	7.85	0.013 / fixed	1.01 ± 0.12	8.5/10	5.00
25	0.60 ± 0.05	2.34 ± 0.33	1.5/5	5.02	0.30 ± 0.10	1.05 ± 0.17	2.9/5	4.34
27	0.37 ± 0.17	2.90 ± 0.88	4.9/4	3.11	0.19 ± 0.10	0.49 ± 0.12	4.9/4	2.30
35	0.63 ± 0.09	3.74 ± 0.34	19.6/22	10.75	0.33 ± 0.05	0.49 ± 0.04	17.4/22	8.96

[a] Errors are quoted at the 90% confidence level.

model provides an acceptable fit ($\chi^2/{\rm dof} = 63.4/51$), with a gas temperature of 0.30 ± 0.02 keV and a photon index of 2.47 ± 0.26 . The total flux of the emission in 0.3–10.0 keV is 7.24×10^{-13} erg s^{-1} cm^{-2}, of which about 54% can be ascribed to the power-law component.

Of the 43 X-ray sources resolved within $2R_{\rm e}$, 10 sources (Src 1, 5, 8, 9, 16, 18, 22, 25, 27 and 35) have total counts greater than 100. We extracted the individual spectra of these sources and the corresponding background spectra in annular regions adjacent to where the source spectra were extracted. We fitted each spectrum with an absorbed power-law model and/or an absorbed multicolor disk blackbody model (DBB), and list the results in Table 2. The spectrum of the central source (Src 1) is well fitted by an absorbed power-law model with a photon index of 1.61 ± 0.15, which is typical of supermassive black holes in active galaxies. The 0.3–10.0 keV luminosity of Src 1 corrected for the absorption is calculated to be 3.16×10^{38} erg s^{-1}, which is lower than that of most low-luminosity AGNs. The spectrum of the brightest source Src 35, which showed significant temporal variations during the observation (Sect.4.2), can be fitted with an absorbed DBB model with an inner disk temperature of $kT_{\rm in} = 0.49 \pm 0.04$ keV. This source is a candidate ultra-luminous X-ray source (ULX) since its 0.3–10.0 keV luminosity is 1.25×10^{39} erg s^{-1}.

According to previous studies of SSSs in spiral galaxies (e.g., M101, Pence et al. 2001; M31, Kong et al. 2002; M83, Soria & Wu 2003), SSSs are probably white dwarfs fueled by accretion from their low-mass companions. Indeed we find that the spectrum of the SSS candidate Src 9 can be fitted with an absorbed DBB model with the inner temperature of 0.15 ± 0.01 keV, which is consistent with that of an accreting white dwarf.

4.5 X-Ray Luminosity Functions of the Resolved Off-Center Point Sources

4.5.1 All Off-Center Sources Detected within $2R_{\rm e}$

Assuming that all the off-center X-ray point sources resolved within $2R_{\rm e}$ are located at the distance of NGC 5055, we calculated their X-ray luminosities in 0.3–10.0 keV using the best-fit spectral parameters for their cumulative spectrum. The conversion factor of the counts is 2.13×10^{36} erg cts^{-1}, and the resulting luminosities range from 2.1×10^{37} to 1.25×10^{39} erg s^{-1}. With these we construct the XLF and illustrate it in Figure 5a. Since the detection of the point sources is not complete at the faint end of the luminosity function, by adopting a method similar to that utilized in, e.g., Kim & Fabbiano (2004) and Xu et al. (2005) we ran Monte-Carlo simulations to create fake point sources on the S3 image of NGC 5055 in 0.3–10.0 keV. In the simulations we created fake sources by using the MARX package (Wise et al. 1997), and assumed that the radial distribution of the fake sources at any given luminosity follows the r$^{1/4}$ law (de Vaucouleurs 1948). At a given luminosity, we determined how many of the fake sources can be detected with the same technique used in Section 4.1. In such a way we corrected both the observed XLF and the background for the unresolved sources. The corrected XLF are also shown in Figure 5b.

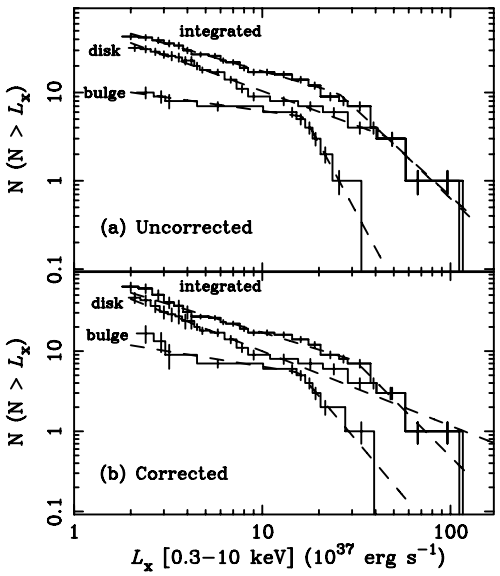

Fig. 5 XLFs of the detected off-center X-ray point sources uncorrected (a) and corrected (b) for incompleteness at the low luminosity end. Models are plotted as dashed lines. A single power-law model is sufficient to describe the corrected XLF of the disk population, while in other cases a broken power-law model is needed (Sect.4.5).

We fitted both the uncorrected and corrected cumulative XLFs with the software Sherpa for either a single power-law profile or a broken power-law profile,

$$N(>L) = N_0 \begin{cases} (L/L_{38})^{-\alpha_l} & L < L_b \\ (L_b)^{\alpha_h-\alpha_l}(L/L_{38})^{-\alpha_h} & L > L_b \end{cases},$$

where L/L_{38} is the 0.3–10.0 keV luminosity in units of 10^{38} erg s^{-1}, α_l and α_h are the slope indices for the lower and higher luminosity ends, respectively. We find that for the uncorrected XLF, fitting with the single power-law model can be immediately rejected ($\chi^2/\mathrm{dof} = 150.2/21$). It overestimates the data at high luminosities and underestimates the data at low luminosities. The use of the broken power-law model, on the other hand, can significantly improve the fit and provide us with an acceptable fit ($\chi^2/\mathrm{dof} = 15.8/19$). The best-fit parameters at the 90% confidence level are $L_b = 2.53^{+0.56}_{-0.45} \times 10^{38}$ erg s^{-1}, $\alpha_l = 0.61^{+0.02}_{-0.03}$ and $\alpha_h = 1.96^{+0.58}_{-0.18}$. For the XLF corrected for the effect of incompleteness at the faint end of the XLF, the single power-law model is again unable to give an acceptable fit ($\chi^2/\mathrm{dof} = 125.8/22$), while the broken power-law model can improve the fit significantly ($\chi^2/\mathrm{dof} = 23.1/20$) with the best-fit parameters $L_b = 3.11^{+0.37}_{-0.48} \times 10^{38}$ erg s^{-1}, $\alpha_l = 0.71 \pm 0.05$ and $\alpha_h = 2.36^{+0.54}_{-0.43}$.

4.5.2 Bulge and Disk Populations

We studied the XLFs of the bulge and disk population sources (Fig. 5) and found that the single power-law model is inadequate to describe both the uncorrected XLFs of the bulge population ($\chi^2/\mathrm{dof} = 68.9/9$) and the disk population ($\chi^2/\mathrm{dof} = 30.3/19$). The broken power-law model, however, gives a good fit to the data with $L_b = 1.68^{+0.12}_{-0.22} \times 10^{38}$ erg s^{-1}, $\alpha_l = 0.31 \pm 0.12$ and $\alpha_h = 3.95^{+1.44}_{-1.19}$ for the bulge population ($\chi^2/\mathrm{dof} = 7.4/7$), and $L_b = 3.11^{+0.37}_{-0.48} \times 10^{38}$ erg s^{-1}, $\alpha_l = 0.71 \pm 0.05$ and $\alpha_h = 2.36^{+0.54}_{-0.43}$ for the disk population ($\chi^2/\mathrm{dof} = 23.1/20$). We then corrected the XLFs for incompleteness at the low energies using the method described above for all the resolved off-center sources. For the bulge population, a broken power-law is still needed to describe the XLF with $L_b = 1.57^{+0.21}_{-0.20} \times 10^{38}$ erg s^{-1}, $\alpha_l = 0.38^{+0.20}_{-0.23}$

and $\alpha_h = 2.28^{+1.30}_{-0.65}$ ($\chi^2/\mathrm{dof} = 7.4/7$). The corrected XLF of the disk population is found to be nicely consistent with a single power-law model with a slope of $\alpha = 0.93^{+0.07}_{-0.06}$ ($\chi^2/\mathrm{dof} = 16.3/19$).

We have crosschecked our results on the XLF profiles of all the resolved, off-center sources and disk population by excluding Src 35, the brightest source that may bias the fittings. We found that within the errors the best-fit parameters are consistent with those obtained with Src 35 included.

5 DISCUSSION

We calculated the 0.3–10.0 keV luminosities of 43 X-ray point sources detected within $2R_{\rm e}$ of NGC 5055 and found that they span a wide range from about 2.1×10^{37} erg s^{-1} to 1.25×10^{39} erg s^{-1}, which is typical for spiral galaxies (M81, Tennant et al. 2001; NGC 1637, Immler et al. 2003) and early-type galaxies (Xu et al. 2005 and references therein) at similar distances. After compensating for the incompleteness at the low luminosity end, we found that the corrected XLF of the bulge population is well fitted with a broken power-law model, while the profile of the disk population's XLF satisfies a single power-law distribution. The disk population is significantly richer at the high-luminosity end ($\gtrsim 2 \times 10^{38}$ erg s^{-1}) than the bulge population, indicating that the star formation history of the bulge is distinct from that of the disk. In other words, the disk may have undergone recent, strong starbursts that significantly increased the HMXB population, although ongoing starbursts are also observed in the nuclear region of NGC 5055. A quite similar phenomenon has been found in M81 (also identified as a LINER or Sy1.8) by Tennant et al. (2001), who reported that the XLF of the bulge population exhibits a break at $\sim 4 \times 10^{37}$ erg s^{-1}, and the XLF of the disk population can be fitted with a single power-law.

Different patterns of spatial variation of XLF profiles for the bulge and the disk are observed in other spiral galaxies. In M83, a SAB(s)c galaxy that hosts a starburst nucleus (Soira & Wu 2003), the bulge XLF profile is consistent with a single power-law with a slope of 0.8, while a break appears on the XLF of the disk population at about 8×10^{37} erg s^{-1}. This might suggest that, unlike NGC 5055 and M81, there is no strong starbursts in M83 on the disk in the recent past, and the HMXBs dominate the source population only in the nuclear starburst regions, rather than over the entire disk. In M31, Primini et al. (1993), Shirey et al. (2001), Kaaret (2002) and Kong et al. (2002) found that the cumulative XLF of all the detected point sources has a distinct break at $(2-3) \times 10^{37}$ erg s^{-1}, a slope of 1.36 ± 0.33 for the high luminosity end and a slope of 0.47 ± 0.09 for the low luminosity end. Kong et al. (2002) also studied the cumulative XLFs of the point sources in the inner bulge, outer bulge and disk regions. They found that there is a spatial variation in the XLF profiles; both the break luminosity and the slope of the cumulative XLF increase outwards monotonously from the inner bulge, where the LMXBs dominate the X-ray emission of point sources, to the disk. In a few other spiral galaxies where the XLFs have been studied in detail, however, the report of a break on the XLF is not available in literature. These includes M101 (Pence et al. 2001), IC342 (Bauer et al. 2003; Kong 2003), NGC 891 (Temple et al. 2005), NGC 1637 (Immler et al. 2003) and M51 (Terashima & Wilson 2004), for which the slopes of the XLFs range from about 0.5 to about 1.

The diversity of the XLF profiles of the X-ray sources in spiral galaxies indicates that the star formation and evolution history may be more complex than we have expected, so that further careful multi-band investigations are needed. In addition, we suggest that, since typically only 50–150 X-ray point sources are detected in a given galaxy, the uncertainty introduced by the small number statistics may bias our conclusions on the XLF profile to a certain extent. By Monte-Carlo simulations Xu et al. (2005) showed that even if there is a universal break on the XLFs of early-type galaxies, the statistical errors definitely preclude us from measuring it correctly. The same result can be applied to the measurements of the XLF profiles of spiral galaxies.

6 SUMMARY

We detected a total of 43 X-ray point sources (12 in the bulge and 31 on the disk) within two effective radii of NGC 5055. Their 0.3–10.0 keV luminosities range from a few times 10^{37} erg s^{-1} to over 10^{39} erg s^{-1}. After compensating for incompleteness at the low luminosity end, the corrected XLF of the bulge population is well fitted with a broken power-law model ($L_b = 1.57^{+0.21}_{-0.20} \times 10^{38}$ erg s^{-1}), while the XLF of the disk population satisfies a single power-law distribution ($\alpha = 0.93^{+0.07}_{-0.06}$). The disk population is significantly richer at $\gtrsim 2 \times 10^{38}$ erg s^{-1} than the bulge population, indicating that the disk may have undergone relatively recent, strong starbursts that significantly increased the HMXB population, although ongoing starbursts are

also observed in the nuclear region. This is similar to what has been found in M81. In most other spiral galaxies, however, different patterns of the spatial variation of the XLF profiles from the bulge to the disk are observed, indicating that the star formation and evolution history may be more complex than we have expected.

Acknowledgements This work was supported by the National Natural Science Foundation of China (NSFC, Grants 10273009 and 10233040), and Shanghai Key Projects in Basic Research No. 04JC14079.

References

Baggett W. E., Baggett S. M., Anderson K. S. J., 1998, AJ, 116, 1626
Bauer F. E., Brandt W. N., Lehmer B., 2003, AJ, 126, 2797
de Vaucouleurs G., 1948, Ann. d'Astrophys., 11, 247
Dickey J. M., Lockman F. J., 1990, ARA&A, 28, 215
Elmegreen D. M., Elmegreen B. G., 1987, ApJ, 314, 3
Garcia-Gomez C., Athanassoula E., 1991, A&AS, 89, 159
Immler S., Wang Q. D., Leonard D. C. et al., 2003, ApJ, 595, 727
Kaaret P., 2002, ApJ, 578, 114
Kahabka P., 1999, A&A, 344, 459
Kahabka P., 2002, A&A, 388, 100
Kim D.-W., Fabbiano G., 2004, ApJ, 611, 846
Kong A. K. H., 2003, MNRAS, 346, 265
Kong A. K. H., Garcia M. R., Primini F. A. et al., 2002, ApJ, 577, 738
Leitherer C., Li I.-H., Calzetti D. et al., 2002, ApJS, 140, 303
Maoz D., Filippenko A. V., Ho L. C. et al., 1996, ApJS, 107, 215
Maoz D., Koratkar A., Shields J. C. et al., 1998, AJ, 116, 55
Michele D. V., Serra R., 1997, Met, 3, 26
Mushotzky R. F., Cowie L. L., Barger A. J. et al., 2000, Nature, 404, 459
Pence W. D., Snowden S. L., Mukai K. et al., 2001, ApJ, 561, 189
Primini F. A., Forman W., Jones C., 1993, ApJ, 410, 615
Sarazin C. L., Irwin J. A., Bregman J. N., 2000, ApJ, 544, L101
Shirey R., Soria R., Borozdin K. et al., 2001, A&A, 365, L195
Soria R., Kong A. K. H., 2002, ApJ, 572, L33
Soria R., Wu K., 2003, A&A, 410, 53
Supper R., Hasinger G., Pietsch W. et al., 1997, A&A, 317, 328
Swartz D. A., Ghosh K. K., Suleimanov V. et al., 2002, ApJ, 574, 382
Temple R. F., Raychaudhury S., Stevens I. R., 2005, MNRAS, 362, 581
Tennant A. F., Wu K., Ghosh K. K., 2001, ApJ, 549, L43
Terashima Y., Wilson A. S., 2004, ApJ, 601, 735
Thornley M. D., 1996, ApJ, 469, L45
Tyler K., Quillen A. C., LaPage A. et al., 2004, ApJ, 610, 213
Wise M. W., Huenemoerder D. P., Davis J. E., 1997, ASPC, 125, 477
Xu Y.-H., Xu H.-G., Zhang Z.-L. et al., 2005, ApJ, 631, 809